



Cite this: DOI: 10.1039/c7ce00880e

Super-long ZnO nanofibers and novel nucleation mechanism for a gas-phase environment: spatial linear nucleation

 Xiaopeng Yang,^{id}*^a Feng Liu,^a Guangbin Duan,^a
Bingqiang Cao^a and Liqiang Zhang^b

Single-crystal super-long ZnO nanofibers (SZFs) have been prepared *via* a purposely designed vapor transport process. To understand the growth process, a novel freestanding crystal nucleation mechanism, spatial linear nucleation (SLN), is proposed. The contrast experiments show that the SLN process and crystal growth rate are faster than that of classical mechanisms due to the higher gas supersaturation condition and proper Zn/O ratio. We also find that, for freestanding nucleation, Zn-rich conditions facilitate spatial dot nucleation to form tetrapod-shaped ZnO (T-ZnO), however, O-rich conditions favor SLN and nanofiber growth when the concentration of the reactants is high enough. The SLN process depends strongly on factors such as an ultra-high reactant concentration and an appropriate reactant ratio and temperature. For further proving the validity of the SLN mechanism, molecular dynamics (MD) and geometry optimization (GO) calculations based on first principles were carried out. The results of the calculations demonstrate that the spontaneous oriented attachment of metastable primary nuclei in gas-phase environments is feasible to realize spatial linear nucleation.

 Received 9th May 2017,
Accepted 23rd July 2017

DOI: 10.1039/c7ce00880e

rsc.li/crystengcomm

Introduction

For the past few decades, nanoscale materials have represented a new class of materials. They are touted as alternatives to current thin film semiconductors and their manufacture relies on new technologies. Various reasonable crystal nucleation and growth mechanisms for nanostructures in gas-phase environments have been presented to understand the crystal growth process and to aid their design. The most well-known mechanisms are the vapor–liquid–solid (VLS),^{1–3} vapour–solid (VS),^{4,5} vapor–solid–solid (VSS),^{6–8} oxide-assisted growth (OAG),^{9–11} and self-catalytic growth (SCG)^{12,13} mechanisms. However, almost all of these existing mechanisms focus on the crystal growth process rather than an initial nucleation process based on phase transitions and molecular kinetics or thermodynamics. For example, the crystal growth processes of MgO nanorods on a substrate^{2,3} and tetrapod-like ZnO (T-ZnO) nanostructures in the vapor phase^{4,5,14} can both be interpreted using VS mechanisms. However, their nucleation processes are dramatically different. The former is

dependent on the substrate, which can significantly decrease the thermodynamic barrier for the formation of the primary clusters, so it is heterogeneous nucleation. The nucleation process of the latter finishes in the gas phase without a exotic seed crystal as the nucleus, so it is homogeneous nucleation. Nanowires are another example and they can be prepared *via* the VLS process using a metal catalyst,^{15,16} and T-ZnO nanostructures have also been made *via* the VLS process.¹⁷ However, their nucleation routes are dramatically distinct from each other, as the former reaction has a much lower nucleation barrier. Therefore, there are many key problems that are still unclear despite there being a great deal of work on crystal nucleation and growth, especially for homogeneous nucleation crystallization that occurs in the gas phase without a substrate offering nucleation centers.

For ZnO nanostructures, the number of studies based on homogeneous nucleation mechanisms is far less than the number of studies based on heterogeneous nucleation. Homogeneous nucleation is more sensitive to the initial conditions, such as the reactant ratio and concentration, reaction temperature, homogeneous nucleation rate, saturation, *etc.*¹⁸ When it comes to freestanding ZnO nanostructures, it is usually the growth processes that are analyzed in detail, leaving the nucleation mechanisms unknown, and this is true for examples such as nanobelts,¹⁹ nanosprings²⁰ and even nanowires.²¹ We all know that crystal nucleation processes are essential but different to crystal growth processes. Therefore,

^a Materials Research Center for Energy and Photoelectrochemical Conversion, School of Material Science and Engineering, University of Jinan, Jinan 250022, Shandong, China. E-mail: mse_yangxp@ujn.eud.cn

^b State Key Laboratory of Heavy Oil Processing and Department of Materials Science and Engineering, China University of Petroleum, Beijing 102249, China

gaining a deeper knowledge of these mechanisms is of considerable basic and practical significance.²²

In this work, we prepared super-long (centimeter-scale) ZnO nanofibers (SZFs) under unique reaction conditions using a chemical vapor deposition (CVD) method. Their length–diameter (LD) ratio is greater than 1463. Based on a set of contrast experiments and thermodynamics analyses, a novel crystal nucleation mechanism, the spatial linear nucleation (SLN) mechanism, is proposed, which is different to existing freestanding nucleation models. The SLN process relies on factors such as an ultra-high reactant concentration, an appropriate reactant ratio and an appropriate temperature.

Experimental

Fig. 1(a) is a schematic illustration of the experimental set-up for the ZnO nanostructure preparation, which shows a horizontal tube furnace with a quartz-plate-covered quartz boat placed in the constant temperature zone of the furnace. 3 g of ZnO powder and 3 g of graphite powder were ground together for 2 hours and transferred to the left side of the quartz boat to be used as the material sources. A frosted quartz plate was placed on top of the boat to prevent the Zn vapor from oxidizing too rapidly. The green solid lines in the figure indicate the location and the general shapes of the SZFs. The diffusion paths of the Zn vapor and N₂/O₂ are indicated using green and purple dashed lines with arrows, respectively. The depth of the quartz boat is 3 cm. Fig. 1(a) also shows the three zones where the ZnO nanostructures grew, zone A, B and C. Fig. 1(b) shows a sketch of the chemical vapor transport process of the reactant diffusion (Zn vapor and O₂) in the quartz boat. The big dark green and small orange dots denote Zn and O, respectively. Zone A, the dark green area, denotes the Zn-rich zone and zone C, the purple area, is the O-rich zone. Fig. 2 shows a diagram of the actual experiment time dependency on the reaction concentration and actual system pressure (P_{sys}) in the quartz boat. It includes two sets of curves, displayed using solid and dashed lines. The

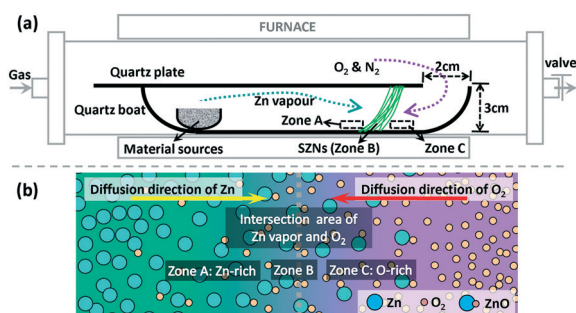


Fig. 1 (a) Schematic illustration of the chemical vapor transport and experimental set-up for the SZF growth. The green solid lines located at zone B are the SZFs. The diffusion paths of the Zn vapor and O₂ are indicated using dashed arrows. (b) A sketch of the reactant diffusion process in the quartz boat.

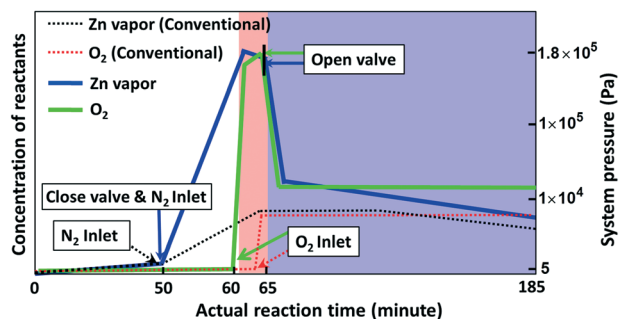


Fig. 2 Diagram of the reactant concentrations with actual experiment time and system pressure in the quartz boat. The right vertical axis shows the corresponding system pressure. The red area represents the nucleation stage (including the first order phase transition and second order phase transition stages) and the blue area represents the crystal growth stage.

set of solid lines represents the Zn vapor and O₂ concentrations with actual time changes under our unique dynamic reaction (UDR) conditions. In the first 50 minutes of the UDR, the tube furnace was evacuated to reach a system base pressure of ~ 1 Pa, and then the pumping valve was closed. In the meantime, N₂ was continuously introduced into the furnace with a very large flow rate (400 sccm). Thus, the Zn vapour was sealed in the quartz boat and reached the maximum concentration after 10 minutes. At the 60 minute point, O₂ was introduced with a flow rate of 40 sccm and the P_{sys} value reached its maximum ($\sim 1.8 \times 10^5$ Pa). After the above non-equilibrium processes, much higher levels for the Zn and O concentrations could be achieved than those using conventional methods. Thus, the time from 60 to 65 minutes (the red area in Fig. 2) should be the main reaction and nucleation stage, as it has an extraordinarily high Zn vapor and O concentration. At the 65 minute point, the N₂ and O₂ flow rates were decreased to 100 and 2 sccm, respectively, corresponding to the blue area, which indicates the VLS crystal growth process. The set of dashed lines denotes the Zn vapor and O₂ concentrations with the actual time changes under conventional static reaction (CSR) conditions. In the CSR, when the P_{sys} value was pumped to ~ 1 Pa at the 50 minute point, N₂ was introduced into the furnace with a flow rate of 100 sccm. Then, the pumping valve was adjusted to keep the P_{sys} value at 5×10^3 Pa until the end of the experiment. Once the P_{sys} value reached 5×10^3 Pa, O₂ was flowed with a 2 sccm flux. In the CSR process, there is no clear line of demarcation between the nucleation and crystal growth stages, and the concentrations of the reactants were always maintained at lower levels than those in the UDR process.

Experiment 1

The T-ZnOs and SZFs were prepared under UDR conditions using a thermal evaporation method on the bottom of the quartz boat, as shown in Fig. 3 and 4. The reaction was carried out in the quartz-plate-covered boat, as shown in Fig. 1a.

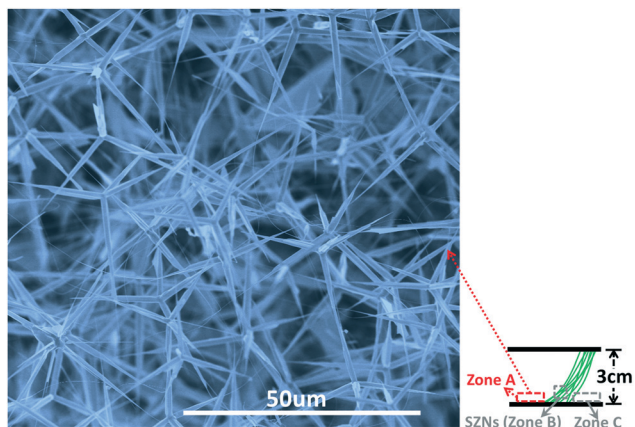


Fig. 3 SEM image of the T-ZnO nanostructures in zone A of the quartz boat in experiment 1 and a schematic illustration of zone A of the quartz boat, where the T-ZnOs grew.

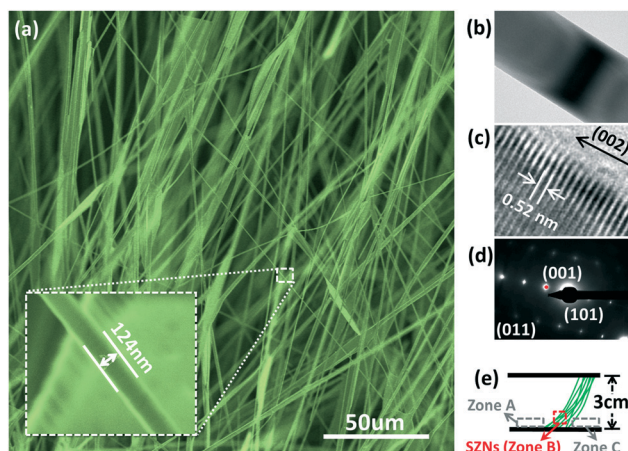


Fig. 4 (a) SEM images of the SZF nanostructures from zone B of the quartz boat in experiment 1. The inset image is the magnification of one nanofiber. (b) A TEM image of one of the SZFs. (c) An HRTEM image of the nanofiber shown in image b. (d) The corresponding SAED pattern of the nanofiber in image c. (e) A schematic illustration of zone B of the quartz boat, where the SZFs grew.

At the beginning, the system pressure (P_{sys}) was pumped to ~ 1 Pa. The temperature (T) of the furnace was ramped up to 1000 °C at a rate of 20 °C min^{-1} . To get a high concentration of zinc vapor, the vacuum pump valve was closed when the temperature reached 1000 °C. Simultaneously, N_2 was introduced into the chamber continuously at a flow rate of 250 sccm. Thus, the Zn vapor was enclosed in the boat by the raising the value of P_{sys} . When the P_{sys} value reached 1.5×10^5 Pa, O_2 was introduced into the furnace with a flow rate of 40 sccm as the reaction gas. When $P_{\text{sys}} > 1.8 \times 10^5$ Pa, the valve was opened and the P_{sys} value was kept at 8×10^4 Pa for 1 hour (N_2 : 100 sccm and O_2 : 2 sccm). Fig. 1(b) demonstrates the diffusion processes of the Zn vapor and O_2 in the quartz boat with the probable Zn-rich and O-rich zones marked. By using this experiment, we synthesized uniform T-ZnO in zone A and SZF nanocrystals in zone B, as shown in Fig. 3 and 4.

Experiment 2 (contrast experiment)

A contrast experiment was carried out under the CSR conditions, shown as dashed lines in Fig. 2. When the P_{sys} value and temperature reached ~ 1 Pa and 1000 °C, respectively, N_2 was flown into the furnace at a 100 sccm flow rate. Then, the pumping valve was adjusted to keep the P_{sys} value at 5×10^3 Pa until the end of the experiment. Once the P_{sys} value reached 5×10^3 Pa, O_2 was introduced with a flux of 2 sccm for 1 , 1.5 , and 2 hours, respectively. Finally, ZnO nanorod arrays (ZNAs) were prepared, as shown in Fig. 5.

The morphologies of the prepared T-ZnOs, SZFs, and ZNAs were analyzed using scanning electron microscopy (SEM) (Hitachi 4800s). The crystal structures of the products were identified using high resolution transmission electron microscopy (HRTEM, FEI F20). Room temperature PL measurements were carried out using a He–Cd laser with 325 nm excitation to evaluate the optical properties. The O $1s$ core-level spectra of the T-ZnOs and SZFs were recorded using X-ray photoelectron spectroscopy (XPS) and calibrated using the C $1s$ peak.

To further prove the validity of our proposed SLN mechanism, molecular dynamics (MD) and geometry optimization (GO) calculations based on first principles were carried out using the Dmol3 package. In all of our simulations, we used relativistic all electron DFT total energy methods. In the MD calculations, the Perdew–Wang exchange correlation functional²³ within the local-density approximation (LDA) was used. The Monkhorst–Pack grid of $3 \times 3 \times 2$ k -points was chosen for the Brillouin zone sampling in the final geometry optimization calculation, which was carried out with the generalized gradient approximation (GGA) and the Perdew–Burke–Ernzerhof scheme to treat the exchange–correlation function. The energy cut off for the plane-wave expansion was set to 380 eV and the valence atomic configurations were $3d^{10}4s^2$ for Zn and $2s^22p^4$ for O.

Test analysis

Fig. 3 shows an SEM image of the T-ZnO nanostructures in zone A of the quartz boat in experiment 1. Based on Fig. 3, one leg of the T-ZnO nanostructures is about 30 – 50 μm , which is much longer than values of 0.2 – 2 μm in existing reports.^{5,24–26} It may be caused by the ultrahigh reactant concentrations in the UDR process compared to those in the CSR process. So, we can speculate that the reactant

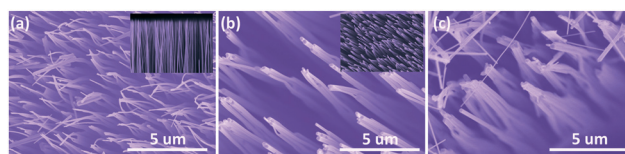


Fig. 5 SEM images of the ZNAs in experiment 2. (a) Grown for 1 hour, the inset is the cross-section image; (b) grown for 1.5 hours, inset is a low magnification image; and (c) grown for 2 hours.

concentration will influence the size rather than the shape of the nanostructures. These T-ZnO nanocrystals consist of a ZnO core in the zinc blende structure, from which four ZnO arms in the wurtzite structure radiate.²⁵

Macroscopically, the SZFs have the shape of scattered fiber bundles, stretching from the bottom of the quartz boat to the quartz plate on top, as shown in Fig. 4(e) and 1(a). The distance between the top and the bottom of the boat is 3 cm. The length of the SZFs is unprecedented for ZnO nanostructures fabrication *via* CVD methods, as it is inexplicable for nanoscale materials to cross such a large macroscale distance without any support from crystal nucleation and growth aspects. Microscopically, based on the SEM images in Fig. 4(a), the SZFs are generally smooth and even, with diameters in a wide range of ~ 110 to ~ 2000 nm. The inset of Fig. 4(a) shows the magnification of one of the SZFs with a diameter of 167 nm. Its LD ratio is greater than 1463. Such ZnO nanowires with a high LD ratio have not been reported previously. From the transmission electron microscope (TEM) image shown in Fig. 4(b), the edge of the SZF is clear and its diameter is uniform. The HRTEM image in Fig. 4(c) indicates that the SZF grew along the *C*-axis. There is no surface coating layer growth, which is the characteristic feature of crystal bottom-up growth at high temperatures. The clear SAED pattern in Fig. 4(d) illustrates a wurtzite (WZ) structure with perfect crystalline qualities and no zinc blende (ZB) structure was found.

Fig. 5(a)–(c) show SEM images of the most typical ZnO nanorod arrays (ZNAs) prepared in experiment 2 for 1, 1.5, and 2 hours, respectively. The ZNAs grew from the bottom of the quartz boat. We know from Fig. 5 that the ZNAs are very uniform with an excellent orientation. The inset in Fig. 5(a) shows a cross-section image of the ZNAs, and the length of a single rod is ~ 20 μm . The inset of Fig. 5(b) shows a low magnification image, which demonstrates the uniformity of the ZNAs in a large area. The most remarkable thing about Fig. 5 is that it shows that the top of the ZnO nanorods coalesce together. The longer the growth time, the greater the coalescing effect. In other words, the nanorods, which grew upwards from the substrate, need to find some physical support so that they can overcome external forces, such as gravity, air-flow disturbance, and surface energy reduction requirements. By coalescing together, these nanorods could prevent to toppling down to the ground. Similar phenomena have even been found in ZnO nanorods as short as ~ 20 nm.²⁷

Fig. 6 shows the room-temperature photoluminescence (PL) spectra of T-ZnO, SZFs and ZNAs, which are normalized using the peaks located at ~ 380 nm. For the T-ZnOs, which are represented by the black curve, there is high broad visible emission located at ~ 490 nm, which is similar to the results reported by Park *et al.*²⁸ and Roy *et al.*⁵ It is the most commonly observed defect emission in ZnO nanostructures, which is ascribed to the single V_{O} ^{29,30} caused by Zn-rich environments. A number of reports have also demonstrated that the nucleation process of T-ZnO happens under Zn-rich conditions.^{5,17,31,32} Hence, the T-ZnO grow zone (zone A) should

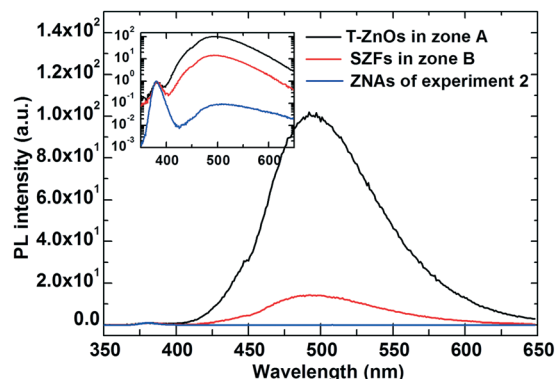


Fig. 6 Room-temperature PL spectra of the T-ZnOs, SZFs, and ZNAs. The inset image is the logarithmic coordinate plot.

be a Zn-rich environment. In addition, zone A is closer to the Zn vapor source than zone B. The lower defect emission of SZFs indicates that SZFs grew in an environment with a relative high proportion of O (zone B). The blue line denotes the PL spectrum of ZNAs prepared in experiment 2. Their visible emission located at ~ 490 nm is rather weaker than that of the T-ZnOs and SZFs by 2 and 3 orders of magnitude, respectively, which means that there are very few V_{O} defects for the ZNAs.

In order to investigate the V_{O} defects of the ZnO nanocrystals, high resolution XPS tests were carried out of O 1s for T-ZnOs and SZFs, as shown in Fig. 7. The O 1s emissions are asymmetric and differ from each other dramatically, indicating that multi-component oxygen species may exist and imbalance each sample. Therefore, three Gaussians were fitted to these spectra: peak 1 (P_{I}) at ~ 530.2 eV, peak 2 (P_{II}) at ~ 531.3 eV, and peak 3 (P_{III}) at ~ 532.5 eV.^{33,34} The peaks were calibrated using the C 1s reference peak at 284.3 eV. The low binding energy, P_{I} , at 529.8 eV was attributed to O_2 -surrounding the ZnO systems.³³ P_{II} was related to oxygen-deficient regions within the ZnO matrix of the ZnO compound. As a result, changes in the intensity of this

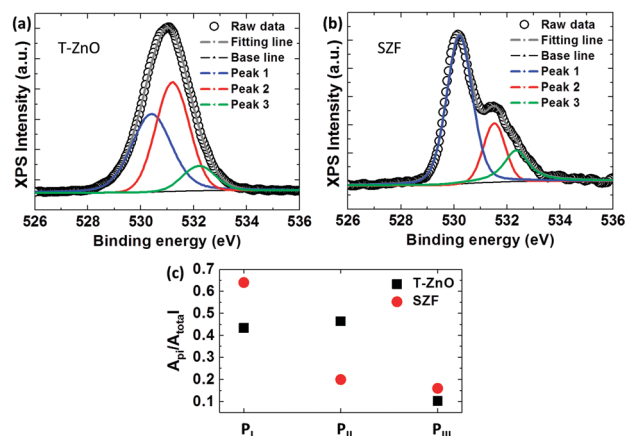


Fig. 7 High resolution XPS spectra of the T-ZnOs and SZFs. (a) The T-ZnOs from zone A, (b) the SZFs from zone B, and (c) the area ratio of P_{I} to the total area of the O 1s peak for the T-ZnOs and SZFs, where *i* denotes I, II, and III.

component may be in connection with the variations in the concentration of the oxygen vacancies (V_O). Therefore, materials with P_{II} are usually considered as green emission sources. Hence, it has a large influence on green emission peak in the PL spectra. The higher binding energy, P_{III} , was associated with loosely bound oxygen containing species on the surface of the nanorods, such as $-CO_3$, adsorbed H_2O , and adsorbed O_2 . The peak area ratios of P_i to the total area (A_{P_i}/A_{total}) are shown in Fig. 7(c), where i denotes I, II, and III. It is found that the values of $A_{P_{II}}:A_{total}$ increase greatly from 0.20 to 0.46 from zone B (SZFs) to zone A (T-ZnOs). Meanwhile, the $A_{P_i}:A_{total}$ values decrease from 0.64 down to 0.43. In other words, the concentration of the V_O defects of the T-ZnOs is much higher than that of the SZFs. This indicates that zone A should be a more Zn-rich or O-poor area compared to zone B, which is beneficial for forming V_O defects. Through the above analysis, the XPS results are consistent with the PL spectra.

Growth mechanism

The nucleation of the ZNAs in experiment 2 should be heterogeneous nucleation, because it is dependent on the substrate. Generally, with the CSR conditions used in experiment 2, the nanofibers/nanowires grew upwards from the substrate in the form of nanorod arrays, and the top of these ZnO nanofibers/nanowires would stick to each other when they were long enough²⁷ (~ 20 μm in our work), which always induced the growth to halt,³⁵ as shown in Fig. 5. Therefore, under CSR conditions, it is impossible to obtain SZFs with an ultra-high LD ratio and an incredible macroscopical span (up to 3 cm from the top of the quartz boat to the bottom). In fact, the heterogeneous nucleation mechanism is relatively simple and well known compared to homogeneous nucleation. Heterogeneous nucleation can even occur at very low reactant concentrations based on the defects on the substrate.³⁶

However, when the initial reactant concentration was big enough, spatial homogeneous nucleation would occur, as shown in Fig. 8(b). Several models have been proposed for the spatial homogeneous nucleation mechanism. For example, for T-ZnOs, it is generally believed that the growth of its arm crystals proceeds based on the nucleation of the core structure.¹⁴ Yu *et al.* have proven the presence of a tetrahedral zinc blende core from which each arm of the tetrapod grows.³⁷ Another successful model, proposed by Takeuchi *et al.*, owing to its agreement with crystallographic measurements,³⁸ is the octa-twin model.³⁹ The authors postulated that a ZnO nucleus is formed from eight tetrahedral crystals, each with three [1122] pyramid facets and one [0001] basal plane facet. These eight tetrahedrons can then be joined together to form a single octahedron, where each basal plane forms a facet of the structure. The present spatial homogeneous nucleation mechanisms for 1D ZnO nanostructures also follow up on the idea that a particle nucleus should be formed as the “seed”, as shown in Fig. 8(c). From what has been mentioned above, the existing nucleation mechanisms

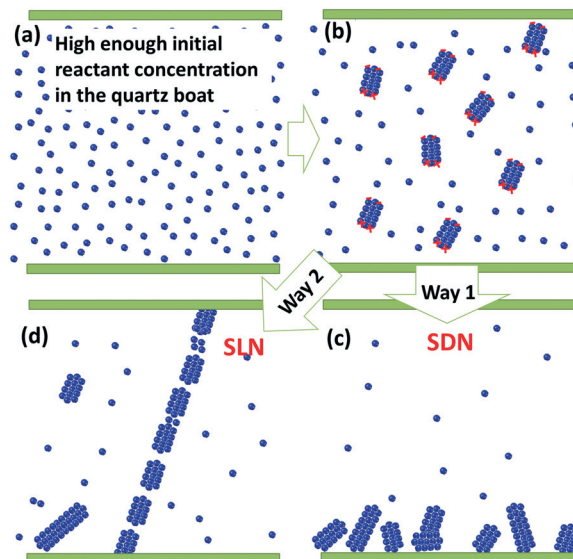


Fig. 8 Schematic of two possible crystal spatial nucleation routes (SDN and SLN) with a high enough initial reactant concentration in the quartz boat. (a) Initial distribution of reactant with high concentration, (b) primary spatial homogeneous nucleation process, (c) traditional SDN process, (d) the newly proposed SLN process.

of crystals in the gas phase have one thing in common, which is that one and only one “seed” must be formed as the growth center for an individual crystal.⁴⁰ Here, we call this spatial dot-like nucleation (SDN). According to the SDN mechanism, the amount of product nanostructures must match the quantity of initial nuclei. Meanwhile, once the nucleation stage is done, it will enter the growth stage and the number of crystals will be fixed. After the growth of the crystals and the sharp reduction of the reactant concentration, the crystals fall towards the substrate as they are subjected to the force of gravity, as shown in Fig. 8(c). This process is just like the formation processes of snow. Therefore, based on the above-mentioned SDN nucleation and growth processes, it is also impossible to interpret the nucleation mechanism of the SZFs in experiment 1, considering their large span from the top of the quartz boat to the bottom (up to 3 cm) and their super large LD ratios.

One might wonder if the nucleation rate would affect the above conclusions when the reactant concentration is ultra-high. The nucleation rate can be expressed as

$$I = n^* \beta \quad (1)$$

where n^* is the average number of critical clusters, and β is the diffusion of the molecules to the cluster. Parameter n^* can be further expressed as

$$N \exp\left(\frac{\Delta G^*}{k_B T}\right)$$

where ΔG^* is the critical free energy needed, corresponding to that of the critical radius, N is the number of potential nucleation sites per unit volume, and k_B is the Boltzmann

constant. The number of clusters with a critical radius r^* is a function of the total number of atoms, n , in the system, the free energy, ΔG , required to create a cluster (of that size), and the temperature, T . Meanwhile, we have

$$N \propto n \cdot \Delta G \cdot T \quad (2)$$

$$\Delta G = -\frac{4}{3}\pi r^3 \Delta G_v + 4\pi r^2 \sigma \quad (3)$$

In our case, T and G are both constants. In other words, the nucleation rate is equal to the number of Zn–O pairs, n . So, when the reactant concentration increased, the number of the nuclei also increased. Thus, under the SDN mechanism, the size of the individual crystal will not increase noticeably, despite the fact that the reactant concentration is increased.

Based on above analysis and our UDR conditions that can provide high reactant concentrations, we propose a novel SLN mechanism, shown as way 2 in Fig. 8 and in more detail in Fig. 9. It features a two-step nucleation process, primary and secondary nucleation, and a one crystal growth process. In particular, the secondary nucleation process forms linear nuclei, which differs from the one-step dot-like nuclei formed *via* SDN. Typically, for spatial nucleation, a first order phase transition starts if a free energy barrier separates the parent phase (the gas phase of Zn, O, and molecular ZnO) from the phase that is thermodynamically more stable (the solid phase of ZnO). Nucleation from this metastable initial state will take place when a rare fluctuation allows the system to surmount the free energy barrier. Although the phase that forms during nucleation must be more stable than the parent phase, it is not necessarily the phase that is the most stable thermodynamically. A metastable phase may nucleate if the transition to that phase is kinetically favored. A phase transition to a thermodynamically stable phase may therefore proceed *via* a two-step process. In the first nucleation event, a metastable intermediate phase is formed; this then goes on to form the final phase *via* a second nucleation event.⁴¹

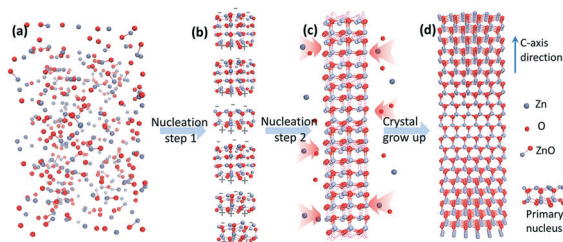


Fig. 9 Schematic diagram of the homogeneous SLN mechanism presented in this article and its VLS crystal growth process in the gas phase. (a) Large amounts of ZnO molecules are produced instantaneously at 1000 °C when O₂ was flown into the furnace, (b) initial nucleation to produce metastable primary nuclei produce at the initial nucleation stage, (c) the secondary nucleus process, (d) the crystal grown up process after the secondary nucleation.

Fig. 9 shows a schematic diagram of the homogeneous SLN mechanism and subsequent VS crystal growth process. In our case, when O₂ was flown into the furnace with a huge flux of 40 sccm, the Zn vapor was oxidized and very large ZnO molecules are produced instantaneously, owing to the high reaction temperature of 1000 °C and the large diffusion flux of the reactants, as shown in Fig. 9(a). According to Fick's law, the diffusion flux is given by eqn (4):

$$J = -D \frac{dM}{dx} \quad (4)$$

where J is the net flux of the vapors, D is the diffusion constant, and dM/dx is the concentration gradient of the vapors along the propagation direction.⁴² High initial Zn vapor and O₂ concentrations at zone A and zone C, respectively, mean that there is a large value of dM/dx , leading to a large J value. Hence, the number, N , of produced ZnO molecules would be larger than that under CSR conditions. Based on eqn (1), the nucleation rate, I , under the UDR conditions will be ultra-high. Meanwhile, the temperature (1000 °C) is below the maximum heterogeneous nucleation temperature (melting temperature 1750 °C). Thus, the gas is super cooled and in a nonequilibrium and supersaturation state,⁴³ which is the key driving force for homogeneous nucleation. At this stage, the primary nucleation stage, many tiny wurtzite-structured quasi-linear nuclei grow due to supersaturated precipitation. Meanwhile, the huge O₂ flux induces a reactant distribution fluctuation that allows the system to surmount the free energy barrier to start initial nucleation to produce metastable primary nuclei, as shown in Fig. 9(b). They have a wurtzite structure and are composed of tetrahedral coordinated O²⁻ and Zn²⁺ ions, stacked alternatively along the c -axis. The oppositely charged ions produce positively charged (0001)-Zn and negatively charged (000 $\bar{1}$)-O polar surfaces.²⁰ Therefore, these quasi-linear nuclei have polar charges on their top and bottom surfaces. In order to minimize the energy of the polar surface, these quasi-linear nuclei almost instantaneously attach to each other and become a super-long linear nucleus, which is called the secondary nucleus here, as seen in Fig. 9(c). At this point, the two-step nucleation stage is complete. Fig. 9(d) shows the growth process of the SZFs. It is worth noting that the crystals grow mainly along the radial direction based on the super long core structure, which is different from traditional SDN.

Why do we choose SLN for zone B rather than SDN? The above paragraph points out that the high concentrations of the reactant under our UDR conditions form dense primary nuclei, which provide a close enough distance and high enough number for the primary nuclei to combine together to form secondary linear nuclei. The other crucial requirements are the supersaturation and Zn/O ratio. The supersaturation determines the nucleation and growth rate of the nanostructures when the thermal evaporation method is used.⁴⁴ The relationship between the growth rate and gas supersaturation can be described by eqn (5):⁴⁵

$$S = \frac{\alpha \sigma P_0}{\sqrt{2\pi m \kappa T}} \quad (5)$$

where S is the growth rate, α is the accommodation coefficient, σ is the gas supersaturation, P_0 is the equilibrium pressure, κ is the Boltzmann constant, and T is the absolute temperature. In our case, P_0 was approximately the same for zone A, B and C. Therefore, S is proportional to σ . From this perspective, nanostructures at zone B have the fastest growth rate.

Owing to the different supersaturation and Zn/O ratios, we obtained different nanostructures, the T-ZnOs and SZFs, in zone A and B, respectively, in experiment 1. Zone A and B have been shown to be Zn- and O-rich areas using the above PL and XPS analysis. In other words, the Zn/O ratio is also a key factor for the nucleation and crystal morphologies.^{32,46,47} ZnO would change its preferred orientation from $2\bar{1}\bar{1}0$ to (0001), when the amount of O gradually increases.²⁷ It has been determined experimentally and theoretically that ZnO grows with a strong preference for the (0001) orientation.⁴⁸ This may be the reason why the primary nucleus has a wurtzite structure in zone B, while it has a tetrahedral zinc blende^{17,25,32} structure in zone A, which finally induces different nucleation processes to make SZFs and T-ZnOs, respectively. Considering that the O-terminated (000 $\bar{1}$) polar surface is inert,¹⁹ an excessive proportion of O (O-rich) may suppress the growth of ZnO. Zone C is a relatively O-rich environment compared to zone A and B. Thus, in zone C, no obvious ZnO nanostructures were found.

Since Penn and Banfield presented a novel crystal growth mechanism, the so-called ‘‘oriented attachment (OA)’’ mechanism, in 1998,⁴⁹ there has been a new wave of research on secondary mono-crystalline particles obtained through the attachment of primary particles based on solution-phase environments. Compared to the OA mechanism, the SLN mechanism focuses on the crystal nucleation process instead of the growth process and applies to gas-phase environments rather than solution-phase environments. So, it is hard for us to ob-

serve the SLN process *in situ* or even find any evidence *via* TEM tests. Fortunately, we found a suspended many-legged nanostructure in zone B, as shown in Fig. 10(a). Obviously, its nucleation should be a free-standing process just like it is for T-ZnO. However, unlike the T-ZnO structures, there is a completely straight nanorod (rod A) throughout the whole nanostructure, as shown in Fig. 10(b). Therefore, it is hard to interpret it using the SDN mechanism or other classical nucleation mechanisms. The many-legged structure is a perfect example of our newly proposed SLN mechanism. There are many growth bands (called striations^{50,51}) on the surface of the legs except for rod A. Striations are growth-induced inhomogeneities in the crystal that are aligned along the faceted or non-faceted growth surface or, in the case of faceted growth with step-bunching, are related to the traces of the macro steps.⁵² It is commonly assumed that striations are caused by temporal growth-rate variations⁵³ or lateral growth-rate differences that are always induced by reaction concentration and temperature fluctuations as the growth progresses. In spatial terms, all of the legs are in the same microenvironment at the same time. Therefore, the clear difference in the surface morphology of the striation-free rod A and the other legs indicates that they did not grow at the same time in a similar reaction environment. The nucleation process of rod A must have finished during the homogeneous nucleation stage *via* the SLN mechanism and the other legs grew later from a point defect in the middle of rod A. Based on the above analyses, we reproduced its growth process in Fig. 10(c). Step 1 shows the free-standing linear nucleus process for rod A (SLN), step 2 illustrates the growth of rod A and the precipitate nucleating at a defect on the rod, and step 3 shows a further growth process of the many-legged structure. In this case, two types of nucleation are involved: SLN for rod A and classical heterogeneous nucleation around the point defect.

To further prove the validity of our proposed SLN mechanism, MD and GO calculations were carried out using the Dmol3 package. Fig. 10(d) and (e) show the ball-stick models of two metastable primary nuclei before and after the DM and GO calculations were performed, respectively. Fig. 10(f) and (g) show the corresponding energy isosurfaces of the electrons. The results of the calculations demonstrate that two separated metastable primary nuclei aligned along the c -axis direction would spontaneously get close to each other and finally integrate together. From Fig. 10(g), we know that the O and Zn elements of the two metastable primary nuclei form stable Zn–O chemical bonds. In other words, the spontaneous oriented attachment of metastable primary nuclei in gas phase environments is feasible, which is the core theory of our proposed SLN mechanism.

Conclusions

In conclusion, we prepared SZFs and T-ZnOs under UDR conditions. A novel SLN mechanism is proposed to understand the crystal free-standing nucleation and the growth process

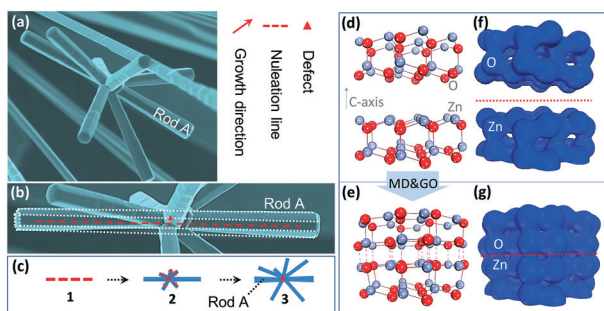


Fig. 10 (a) An SEM image of a many-legged nanostructure located at zone B; (b) a magnified image of rod A; (c) a schematic diagram of the nucleation and growth of the many-legged nanostructure; (d) and (e) show the ball-stick models of two metastable primary nuclei before and after the DM and GO calculations were performed; and (f) and (g) show their corresponding energy isosurfaces of the electrons. The red and gray balls represent O and Zn, respectively.

of the SZFs in gas-phase environments. The SLN mechanism features a two-step nucleation process, primary and secondary nucleation, which differs from the existing nucleation mechanisms due to the existence of a secondary linear nucleus. Three crucial requirements for SLN are discussed: the high reactant concentration, which provides a close enough distance and a high enough number of metastable primary nuclei for it to combine together to form secondary linear nuclei; an appropriate Zn/O ratio, which determines the wurtzite structure of the metastable primary nucleus rather than the tetrahedral zinc blende structure; and the supersaturation condition, which determines whether the nucleation and growth has the fastest rate and provides the driving force in zone B. Different to the SZFs, T-ZnOs were prepared under Zn-rich environments *via* the SDN mechanism. In other words, the ratio and the concentration of the reactants determine the way in which the crystals nucleate. To further prove the validity of the SLN mechanism, molecular dynamics (MD) and geometry optimization (GO) calculations based on first principles were carried out. The results of the calculations demonstrate that the spontaneous oriented attachment of the metastable primary nuclei in gas-phase environments is feasible to realize spatial linear nucleation. We believe that SLN and SDN presented here are helpful for establishing a free-standing (or spatial) crystal nucleation and growth system. Thus, a further study on this would enrich the knowledge on crystal design and growth based on gas-phase environments, and the growth of freestanding nanostructures would be more controllable.

Acknowledgements

This work is supported by the National Natural Science Foundation of China (No. 11404138, 51401239, 21477047), China's Post-doctoral Science Fund (1100512) and Shandong Provincial Natural Science Foundation of China (No. BS2014CL019, ZR2013BL002).

Notes and references

- 1 F. M. Kolb, H. Hofmeister, R. Scholz, M. Zacharias, U. Gösele, D. D. Ma and S. T. Lee, *J. Electrochem. Soc.*, 2004, **151**, G472.
- 2 A. Umar, S. H. Kim, Y. S. Lee, K. S. Nahm and Y. B. Hahn, *J. Cryst. Growth*, 2005, **282**, 131–136.
- 3 P. D. Yang and C. M. Lieber, *J. Mater. Res.*, 1997, **12**, 2981–2996.
- 4 Y. Dai, Y. Zhang, Q. K. Li and C. W. Nan, *Chem. Phys. Lett.*, 2002, **358**, 83–86.
- 5 V. A. L. Roy, A. B. Djurišić, W. K. Chan, J. Gao, H. F. Lui and C. Surya, *Appl. Phys. Lett.*, 2003, **83**, 141–143.
- 6 O. Kryliouk, H. J. Park, H. T. Wang, B. S. Kang, T. J. Anderson, F. Ren and S. J. Pearton, *J. Vac. Sci. Technol., B: Microelectron. Nanometer Struct.–Process., Meas., Phenom.*, 2005, **23**, 1891–1894.
- 7 C. Li, G. Fang, Q. Fu, F. Su, G. Li, X. Wu and X. Zhao, *J. Cryst. Growth*, 2006, **292**, 19–25.
- 8 B. Kim and T. Ritzdorf, *J. Electrochem. Soc.*, 2003, **150**, C577–C584.
- 9 T. Xie, Z. Jiang, G. S. Wu, X. S. Fang, G. H. Li and L. D. Zhang, *J. Cryst. Growth*, 2005, **283**, 286–290.
- 10 C. C. Tang, Y. Bando, Z. W. Liu and D. Golberg, *Chem. Phys. Lett.*, 2003, **376**, 676–682.
- 11 G. S. Cheng, L. D. Zhang, Y. Zhu, G. T. Fei, L. Li, C. M. Mo and Y. Q. Mao, *Appl. Phys. Lett.*, 1999, **75**, 2455–2457.
- 12 S. N. Mohammad, *J. Chem. Phys.*, 2006, 125.
- 13 S. N. Mohammad, *J. Chem. Phys.*, 2007, 127.
- 14 S. L. Yang, R. S. Gao, B. Yang, P. L. Niu and R. H. Yu, *Appl. Phys. A: Mater. Sci. Process.*, 2010, **99**, 9–13.
- 15 Y. W. Wang, L. D. Zhang, C. H. Liang, G. Z. Wang and X. S. Peng, *Chem. Phys. Lett.*, 2002, **357**, 314–318.
- 16 S. N. Mohammad, *Nano Lett.*, 2008, **8**, 1532–1538.
- 17 H. Zhang, L. Shen and S. Guo, *J. Phys. Chem. C*, 2007, **111**, 12939–12943.
- 18 I. J. Ford, *J. Chem. Phys.*, 1996, **105**, 8324.
- 19 Z. L. Wang, X. Y. Kong and J. M. Zuo, *Phys. Rev. Lett.*, 2003, 91.
- 20 X. Y. Kong, Y. Ding, R. Yang and Z. L. Wang, *Science*, 2004, **303**, 1348–1351.
- 21 Z. Chen, N. Wu, Z. Shan, M. Zhao, S. Li, C. B. Jiang, M. K. Chyu and S. X. Mao, *Scr. Mater.*, 2005, **52**, 63–67.
- 22 F. N. Borovik and S. P. Fisenko, *Tech. Phys. Lett.*, 2007, **33**, 151–153.
- 23 J. H. Yuan and K. M. Liew, *Carbon*, 2011, **49**, 677–683.
- 24 F. Wang, Z. Ye, D. Ma, L. Zhu and F. Zhuge, *J. Cryst. Growth*, 2005, **274**, 447–452.
- 25 M. C. Newton and P. A. Warburton, *Mater. Today*, 2007, **10**, 50–54.
- 26 S. L. Yang, R. S. Gao, B. Yang, P. L. Niu and R. H. Yu, *Appl. Phys. A: Mater. Sci. Process.*, 2010, **99**, 9–13.
- 27 S. Li, X. Zhang, B. Yan and T. Yu, *Nanotechnology*, 2009, **20**, 495604.
- 28 K. Park, J. S. Lee, M. Y. Sung and S. Kim, *Jpn. J. Appl. Phys., Part 1*, 2002, **41**, 7317–7321.
- 29 K. Vanheusden, C. H. Seager, W. L. Warren, D. R. Tallant and J. A. Voigt, *Appl. Phys. Lett.*, 1996, **68**, 403–405.
- 30 R. C. Wang, C. P. Liu, J. L. Huang and S. J. Chen, *Appl. Phys. Lett.*, 2005, 87.
- 31 Q. Wan, K. Yu, T. H. Wang and C. L. Lin, *Appl. Phys. Lett.*, 2003, **83**, 2253–2255.
- 32 F. Z. Wang, Z. Z. Ye, D. W. Ma, L. P. Zhu and F. Zhuge, *J. Cryst. Growth*, 2005, **274**, 447–452.
- 33 X. P. Yang, J. G. Lu, H. H. Zhang, B. Lu, J. Y. Huang, C. L. Ye and Z. Z. Ye, *J. Appl. Phys.*, 2012, **112**, 113510.
- 34 R. K. Singhal, P. Kumari, A. Samariya, S. Kumar, S. C. Sharma, Y. T. Xing and E. B. Saitovitch, *Appl. Phys. Lett.*, 2010, **97**, 172503.
- 35 S. Kar, B. N. Pal, S. Chaudhuri and D. Chakravorty, *J. Phys. Chem. B*, 2006, **110**, 4605–4611.
- 36 P. X. G. Yong Ding and Z. L. Wang, *J. Am. Chem. Soc.*, 2004, 7.
- 37 W. D. Yu, X. M. Li and X. D. Gao, *Chem. Phys. Lett.*, 2004, **390**, 296–300.

- 38 Y. Dai, Y. Zhang and Z. L. Wang, *Solid State Commun.*, 2003, **126**, 629–633.
- 39 S. Takeuchi, H. Iwanaga and M. Fujii, *Philos. Mag. A*, 1994, **69**, 1125–1129.
- 40 Z. Chen, Z. Shan, M. S. Cao, L. Lu and S. X. Mao, *Nanotechnology*, 2004, **15**, 365–369.
- 41 J. A. van Meel, A. J. Page, R. P. Sear and D. Frenkel, *J. Chem. Phys.*, 2008, **129**(20), 4069.
- 42 R. Yousefi, M. R. Muhamad and A. K. Zak, *Curr. Appl. Phys.*, 2011, **11**, 767–770.
- 43 K. Yasuoka and M. Matsumoto, *J. Chem. Phys.*, 1998, **109**, 8451–8462.
- 44 C. H. Ye, X. S. Fang, Y. F. Hao, X. M. Teng and L. D. Zhang, *J. Phys. Chem. B*, 2005, **109**, 19758–19765.
- 45 E. Comini, *Anal. Chim. Acta*, 2006, **568**, 28–40.
- 46 B. T. Park and K. Yong, *Nanotechnology*, 2004, **15**, S365–S370.
- 47 C. Y. Leung, A. B. Djuricic, Y. H. Leung, L. Ding, C. L. Yang and W. K. Ge, *J. Cryst. Growth*, 2006, **290**, 131–136.
- 48 N. Fujimura, T. Nishihara, S. Goto, J. F. Xu and T. Ito, *J. Cryst. Growth*, 1993, **130**, 269–279.
- 49 R. L. Penn, *Science*, 1998, **281**, 969–971.
- 50 A. J. Goss, K. E. Benson and W. G. Pfann, *Acta Metall.*, 1956, **4**, 332–333.
- 51 W. Bardsley, J. S. Boulton and D. T. J. Hurle, *Solid-State Electron.*, 1962, **5**, 395–403.
- 52 H. J. Scheel, *J. Cryst. Growth*, 2006, **287**, 214–223.
- 53 P. R. Camp, *J. Appl. Phys.*, 1954, **25**, 459–463.